Recent Developments on Precise Timing with the PICOSEC Micromegas Detector

View the article online for updates and enhancements.

Recent Developments on Precise Timing with the PICOSEC Micromegas Detector

I Manthos[4], J Bortfeldt[2], F Brunbauer[2], C David[2], D Desforge[1], G Fanourakis[5], J Franchi[2], M Gallinaro[7], F García[11], I Giomataris[1], T Gustavsson[9], C Guyot[1], F J Iguaz[1], M Kebbiri[1], K Kordas[4], P Legou[1], J Liu[3], M Lupberger[2], O Maillard[1], I Maniatis[4], H Müller[2], V Niaouris[4], E Oliveri[2], T Papaevangelou[1], K Paraschou[4], M Pomorski[10], F Resnati[2], L Ropelewski[2], D Sampsonidis[4], T Schneider[2], P Schwemling[1], E Scorsone[10], L Sohl[1], M van Stenis[2], P Thuiner[2], Y Tsipolitis[6], S E Tzamarias[4], R Veenhof[8], X Wang[3], S White[2], Z Zhang[3] and Y Zhou[3]

[1] IRFU, CEA, Universite Paris-Saclay, F-91191 Gif-sur-Yvette, France
[2] European Organization for Nuclear Research (CERN), CH-1211 Geneve 23, Switzerland
[3] State Key Laboratory of Particle Detection and Electronics, University of Science and Technology of China, Hefei CN-230026, China
[4] Department of Physics, Aristotle University of Thessaloniki, University Campus, GR-54124, Thessaloniki, Greece.
[5] Institute of Nuclear and Particle Physics, NCSR Demokritos, GR-15341 Agia Paraskevi, Attiki, Greece
[6] National Technical University of Athens, GR-15780, Athens, Greece
[7] Laboratório de Instrumentacão e Física Experimental de Partículas, Lisbon, Portugal
[8] RD51 collaboration, European Organization for Nuclear Research (CERN), CH-1211 Geneve 23, Switzerland
[9] LIDYL, CEA, CNRS, Universit Paris-Saclay, F-91191 Gif-sur-Yvette, France
[10] CEA-LIST, Diamond Sensors Laboratory, CEA Saclay, F-91191 Gif-sur-Yvette, France
[11] Helsinki Institute of Physics, University of Helsinki, FI-00014 Helsinki, Finland

E-mail: ioannis.manthos@cern.ch

Abstract. The PICOSEC-Micromegas detector was developed for precise timing of the arrival of charged particles with a resolution bellow 30 ps. This contribution, after a brief introduction presents results concerning the PICOSEC-Micromegas response to single photoelectrons, estimation of the photoelectron yield of various photocathode types, as well as its performance to time the arrival of test beam muons. In addition, results based on detailed simulation studies and a stochastic model developed for the understanding of the detector are presented. Finally, results of studies related to the development of large scale PICOSEC-Micromegas detector for practical applications are also presented, in particular, the timing performance of a multi-channel PICOSEC prototype.

1. Introduction and detector concept

To meet the needs arising from the high rate environments in current and future High Energy Physics (HEP) experiments, significant advances in the detector technologies are needed. As an
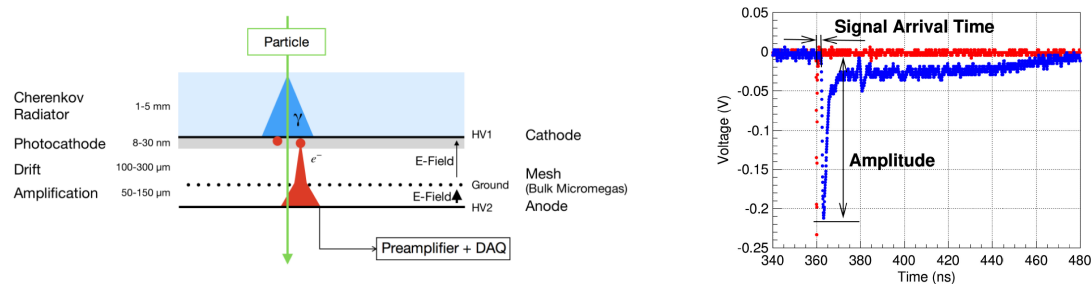
Figure 1. Layout of the PICOSEC-MicroMegas detector (left). Example of a pulse produced by the PICOSEC-Micromegas detector responding to 150 GeV muons (blue), recorded together with the timing reference signal (red) of a microchannel plate (right).

example, in the High Luminocity LHC, any single proton-proton bunch crossing will result in a large number of proton-proton interactions (~ 140) within a small distance ($\sigma \sim 45$ mm). To associate the particles to the correct *pp* interaction vertex, a timing resolution of the order of 30 ps is needed, necessitating the development of new detectors with such timing capabilities.

In this direction, the RD51 PICOSEC-Micromegas collaboration developed a detector [1] (hereafter named PICOSEC) based on the Micromegas technology [2] which has demonstrated timing capabilities below 25 ps [3]. The PICOSEC Micromegas chamber (Fig. 1, left) is coupled to a Cherenkov radiator and a photocathode so that a passing relativistic charged particle produces Cherenkov photons, which subsequently generate prompt electrons in the photocathode. Furthermore the Micromegas drift region is reduced to 200 μm, in order to minimize the probability of ionizations by the passing particle, and to start a pre-amplification avalanche early in the drift region. Results presented here concern single channel anode or segmented anode (multi-pad) PICOSEC bulk Micromegas prototypes, with a mesh-anode distance of 128 μm, with a 3 mm-thick MgF$_2$ layer as a Cherenkov radiator, an 18 nm-thick CsI film as a photocathode, deposited on a 5.5 nm-thick film of semi-transparent Cr serving as the cathode. The gas mixture is the "COMPASS" gas (80% Ne + 10% C$_2$H$_6$ + 10% CF$_4$) at 1 bar.

2. Response to single photoelectrons and muon beams

The electronic response of a single-channel PICOSEC detector to a single photoelectron (single p.e.) is presented in the right plot of Fig. 1. This is a two component signal comprising a fast peak (e-peak) produced by the fast drifting electrons and an extended structure due to the slow moving ions. Single p.e. data were collected at the IRAMIS facility at CEA-Saclay, using a pulsed laser beam. The laser beam was split with one part properly attenuated in order to provide single photon pulses on the PICOSEC, and the other part to illuminate a photodiode used as a time reference with a precision of 13 ps. The performance of the PICOSEC prototypes was also evaluated with 150 GeV muon beam data, collected at the SPS H4 beam line at CERN. In the muon beam test, the time reference was provided by MicroChannel Plates (MCP) with a precision of 4 ps, while the trigger was provided by scintillators. Three GEM detectors were used to track the incident muons, as described in [3]. In all data taking setups mentioned in this contribution, the PICOSEC signal passed through a CIVIDEC pre-amplifier [4] and was digitized by high-bandwidth fast digital oscilloscopes (2.5 GHz LeCroy, 20 Gs/s).

Each PICOSEC digitized waveform was processed offline. The leading edge of the e-peak was fit to a logistic function to reduce noise contribution. A Constant Fraction Discrimination (CFD) technique was applied to the fitted leading edge at the 20% of the e-peak maximum, to time the signal. The Signal Arrival Time (SAT) was defined relative to the time-reference device. The PICOSEC timing resolution is defined as the RMS of the SAT distribution. The
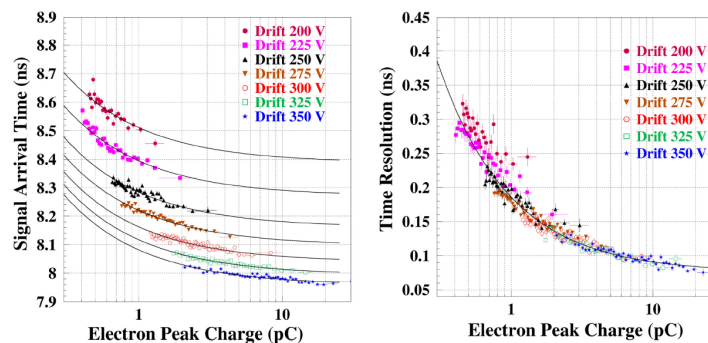
Figure 2. Mean SAT values (left) and timing resolution (right) as a function of the e-peak charge, for single p.e. data, for a fixed anode voltage of +525 V and drift voltages between −200 and −350 V, [3].

whole digitized e-peak waveform was also fit to the difference of two logistic functions and the e-peak charge was estimated by integrating the fitted function.

As already reported [3], the PICOSEC achieved a timing resolution of 76 ± 0.4 ps for single p.e. at +450 V/−425 V anode/drift operating voltages, while when responding to muons it achieved a resolution of 24 ± 0.3 ps for timing the incoming muons, operating at +275 V/−475 V anode/drift voltages. The PICOSEC timing resolution improves when the e-peak charge increases, as observed in both single p.e. and muon data analysis. For example, the right plot of Fig. 2 shows a power law improvement of the resolution in timing single p.e.'s. for different drift voltages. Practically, the timing resolution follows the same dependence on the e-peak charge for any drift voltage. Similarly, as shown in Fig. 2 (left), the mean SAT follows the same power law as a function of the e-peak charge, for all drift voltages. However, it shifts to earlier arrival times for higher drift voltages due to an increased drift velocity. The observed, common power law dependencies, independent of the drift field, is a non-trivial effect; it is not an artifact of the CFD timing technique [3, 5], and must be attributed to the physical mechanism responsible for the signal formation [6].

3. Simulation and modeling

In order to understand the observed dependences of the PICOSEC timing characteristics on the e-peak charge, the Garfield++ [7] detailed simulation was employed. All the relevant processes from the emission of the p.e. from the cathode, up to the transmission of the pre-amplification avalanche electrons through the mesh to the anode region, were simulated. A 2.5 mV RMS uncorrelated electronic noise and the response of the electronics to the amplification avalanche were also included [5]. The simulated pulses were digitized and treated exactly the same way as the experimental waveforms. By applying the same signal processing and analysis to the simulated events, the same dependence of the SAT and the timing resolution on the e-peak charge as in experimental data was found, as it is shown in Fig. 3.

Such an agreement between data and simulation justifies the use of Garfield++ in investigating the microscopic variables which determine the observed signal characteristics. As described in detail [5, 6], it was found that there is a one-to-one correspondence between the e-peak charge and the number of electrons passing through the mesh. In addition, a one-to-one correspondence was found between the SAT and the average of the arrival times of the pre-amplification electrons to the anode region (i.e. time them from the emission of the p.e. till they have just passed through the mesh). The statistical properties of the above time average are determined by the three phases of the signal formation; i. the p.e. drift until it causes the first ionization, ii. the evolution
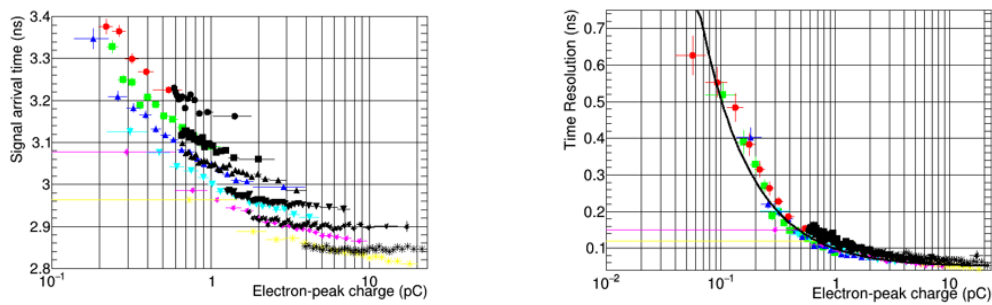
Figure 3. Dependence of the SAT (left) and the timing resolution (right) on the electron peak charge for simulation results to different drift voltages (colour) in comparison with experimental data (black), [5].

of pre-amplification avalanche and iii. the passage of the pre-amplification electrons through the mesh. While the mean transmission time through the mesh is found to be independent of the e-peak charge, both the p.e. and pre-amplification avalanche mean transmission times increase linearly with their respective drift distance. However, it was found that the pre-amplification avalanche drifts with higher velocity than the primary p.e. This means that signals produced by long avalanches arrive earlier (smaller SAT value) than signals produced by shorter avalanches. As the e-peak charge is determined by the number of pre-amplification electrons and this number depends exponentially on the length of the pre-amplification avalanche, this difference in drift velocities causes larger e-peak signals to arrive earlier than smaller ones. Furthermore, as found in the detailed Garfield++ simulation studies [6], the avalanche transmission time depends also, explicitly, logarithmically on the number of the pre-amplification electrons (see next paragraph) due to gains in time at each secondary electron production. Both the above mentioned effects result in avalanches with larger e-peak charges to arrive earlier than avalanches with smaller e-peak charges, with the same functional dependence as observed in the data. In these simulation studies it was also found that the spread of the p.e. transmission time increases with larger drift paths, while the spread of the pre-amplification avalanches transmission time is saturated at a constant value. Therefore, the sooner the primary p.e. ionizes for the first time, the better the timing resolution is (see Fig. 4, right). Due to the correlation of the avalanche length with the number of electrons produced in the avalanche, the spread of the SAT is a decreasing function of the number of the pre-amplification electron as it is shown on the left plot of Fig. 4.

In [6] a phenomenological model is presented, which offers quantitative description of the above observations by employing statistical variables, e.g. drift velocities, multiplication factors, time gains, etc. The model assumes that when a drifting electron losses energy due to inelastic collisions, or when it is produced by ionisation with low kinetic energy, it gains time relative to an energetic electron which undergoes only elastic scatterings. Using this assumption and by including the correlations between the electrons of the pre-amplification avalanche, this model expresses functionally the development of the pre-amplification avalanche, as well as its transmission through the mesh. The model describes the dynamical and statistical properties of the microscopic parameters determining the PICOSEC timing characteristics, in excellent agreement with the detailed simulation predictions (e.g. Fig. 4). It should be emphasized that it predicts not only first and second moments of the relevant microscopic variables, but also their full distributions and it offers phenomenological explanations to the behaviour of the microscopic variables.
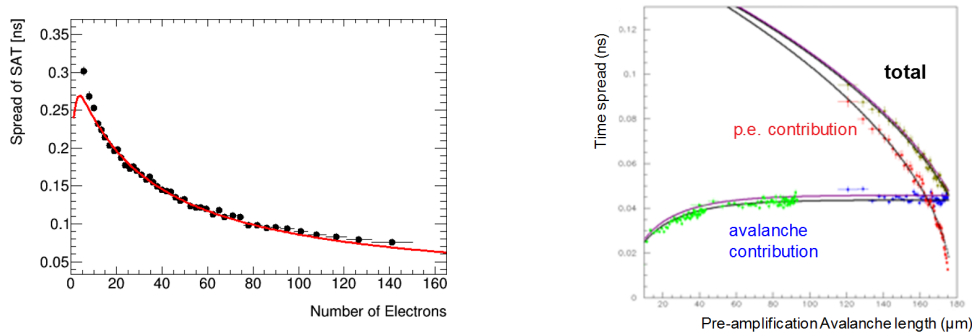
Figure 4. Left: the spread of the total transmission time vs. the number of electrons reaching the mesh. All results are from detailed Garfield++ simulations with anode and drift voltages of +450 V and −425 V, respectively. The lines are not fits to the data but predictions of the model (see text). Right: spread of transmission times vs. pre-amplification avalanche length, for i) the primary p.e. before it ionizes for the first time (red points), ii) the pre-amplification avalanche from its initiation till the mesh (blue points; green points correspond to avalanches which have not yet reached the mesh) and iii) the total transmission time from the creation of the primary p.e. to the arrival of the pre-amplification avalanche to the mesh (black points), [6].

4. Evaluation of the number of photoelectrons per muon track

CsI photocathode used in the PICOSEC test beam runs was found to be damaged after operation. The damage can be caused by the ion back-flow of the generated ions. Exposure in humidity during storage can also damage the photocathode and deteriorate its performance. In a pursuit of immune photocathodes several different materials have been tested [8]. In order to accurately estimate the mean number of p.e's. per muon for a given photocathode, a consistent and unbiased method was developed, which employs the e-peak charge distribution of PICOSEC signals responding to relativistic muons, in comparison with the distribution related to the response of the PICOSEC to single p.e. Indeed, between test beam runs, PICOSEC data were selected using a UV lamp adjusted to illuminate the detector with single photons.

Usually, PICOSEC detectors with circular anode were used in these evaluations. The geometrical acceptance, $A(R)$, of Cherenkov photons produced by a track passing at distance R from the center of the anode is easily evaluated by a toy Monte Carlo, which includes the possibility that photons can be reflected multiple times on both sides of the radiator and they can also be lost. The reflection and absorption probabilities were adjusted so that the geometrical acceptance $A(R)$, to fit the observed dependence of the mean e-peak charge as a function of R as shown in Fig. 5, left. The e-peak charge distribution corresponding to the PICOSEC response to single p.e. from the UV runs, was fitted by a Polya distribution (P_{spe}) determining the mean charge $\bar{Q}_e$ and the shape parameter θ as shown in Fig. 5, right. Assuming that N is the mean value of photoelectrons produced by a muon track, then the probability that N_{pe} photoelectrons are inside the geometrical acceptance of the anode and cause an observed signal, is given by eq. 1. The probability that N_{pe} photoelectrons will give rise to an observed signal of e-peak charge Q, is given by a N_{pe}-fold convolution of P_{spe} terms, as shown in eq. 2. Finally, the probability to observe an event with e-peak charge Q by a track passing at distance R from the anode center, given that the mean value of produced p.e's. is N, is given by eq. 3. Notice that R is a function of the coordinates of the anode center, relative to the tracking reference frame, which in general are unknown. X and Y beam profiles weighted by the observed e-peak charge are used to estimate initial values for the anode center. Then, by fitting eq. 3 to the observed e-peak charge distribution (i.e. as the one shown in the top left plot of Fig. 6), a value for N is estimated. Subsequently, N is fixed and eq. 3 is used again to fit the data, having the
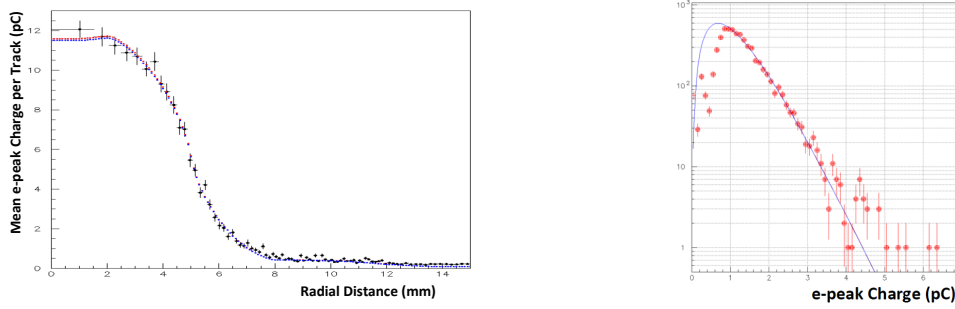
Figure 5. Left: The observed dependence of the mean e-peak charge as a function of R (points), fitted with the geometrical acceptance $A(R)$, the two lines correspond to normalization in two different ranges of the radial distance. Right: The single p.e. charge distribution fitted by a Polya function.

anode center coordinates as free parameter. The procedure is iterated till it converges, offering a simultaneous estimation of the detector position and the number of photoelectrons per muon track.

$$\Pi\left(N_{pe}; N, A\left(R\right)\right) = \frac{[N \cdot A\left(R\right)]^{N_{pe}}}{N_{pe}!} \cdot e^{[-N \cdot A(R)]} \tag{1}$$

$$P\left(Q; N_{pe}, \theta, \bar{Q}_e\right) = \underbrace{P_{spe} \bigotimes P_{spe} \cdots \bigotimes P_{spe}}_{N_{pe} \, times} = \frac{1}{\bar{Q}_e} \frac{(\theta+1)^{N_{pe}(\theta+1)} \left(Q/\bar{Q}_e\right)^{N_{pe}(\theta+1)-1}}{\Gamma\left(N_{pe}\left(\theta+1\right)\right)} \cdot e^{\left[-(\theta+1) \cdot Q/\bar{Q}_e\right]}$$

$$\tag{2}$$

$$F\left(Q, R; N\right) = \sum_{N_{pe}=0}^{\infty} \Pi\left(N_{pe}; N, A\left(R\right)\right) \cdot P\left(Q; N_{pe}, \theta.\bar{Q}_e\right) \tag{3}$$

Fig. 6 (left) shows an example of the e-peak charge distribution for tracks passing up to 6 mm (top) and 3.5 mm (bottom) from the anode center. The red lines are the results of the iterative fit. In this example, it was estimated that the specific CsI photocathode resulted in the production of 11.5 ± 0.4 (stat) ± 0.5 (syst) p.e.'s. per muon track. In Fig. 6 (right) the timing resolution of the detector is shown as a function of R. Assuming that the mean resolution of the detector is proportional to the inverse of the square root of the corresponding mean number of p.e's, the solid curves in Fig. 7 represent a prediction of the dependence of the mean resolution of the track impact when the mean value of the produced photons is 11.5.

5. Towards a large scale device: The multi-channel response to muons

On the way towards large-scale PICOSEC-Micromegas devices, a multi-channel prototype, has been constructed and tested in a muon beam. The anode is segmented in 5 mm-side hexagonal pads and four of them were read-out in a setup identical to the single-pad case. The timing characteristics of each pad vs. the distance R of the track impact point from the pad center, was studied. The average e-peak charge is reduced as the distance R increases. However, the timing resolution and the mean SAT should follow the same dependence on the e-peak charge independently of the distance R. This was not found to be the case, due to geometrical distortions of the chamber which affected locally the drift gap size. Deriving corrections to recover homogeneity and symmetrical behaviour for geometrically equivalent points inside each pad and using them to correct the observed signals, the correct SAT and timing resolution
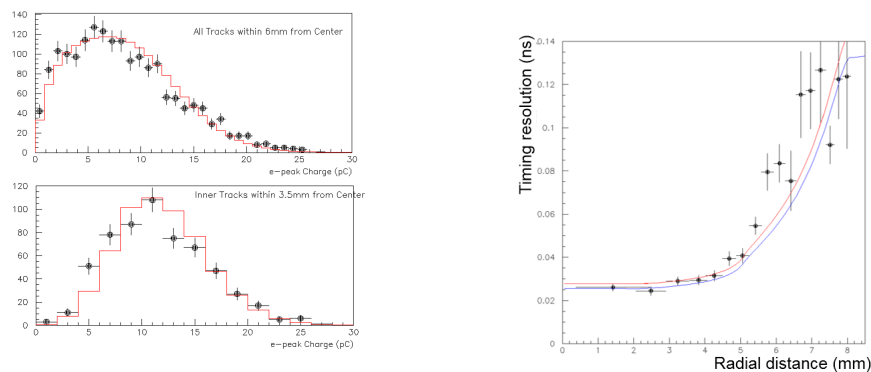
Figure 6. Left: The fit of the described convolution to the charge distribution of the muon beam pulses concerning tracks passing up to 6 mm (top) and 3.5 mm (bottom) from the anode center. The red lines are the results of this fit and the black points represent the experimental data. Right: The timing resolution as a function of the radial distance of the passing muon from the center of the pad is shown as black points. The functional dependence shown in red and blue lines assumes that the timing resolution follows a $1/\sqrt{N \cdot A(R)}$ behaviour. The two lines represent two different normalizations of the same functional dependence.

dependence on the e-peak charge was recovered for each pad. Following the same analysis procedure as for the single pad prototypes, each pad was found to offer a timing resolution of ~ 25 ps, for tracks passing within 2 mm from its center (100% geometrical acceptance). In the region between three pads, where the distance from each pad-center is large, each individual pad accepts a small portion of the Cherenkov cone, resulting to timing resolution in the range of $\sim 70-80$ ps as shown if Fig. 7 (left and top right). A naive combination of the timing information offered by these three neighbouring pads would yield to a combined timing resolution of around 45 ps per muon track. Due to the fact that the arrival time of an individual signal depends on the e-peak charge the individual pad signals should be corrected individually before combined. Furthermore, because the individual pad timing resolution is also a known function of the e-peak charge, the timing information from each pad should be weighted by the related timing resolution. Such a procedure, when applied to this case results to a ~ 30 ps timing resolution (bottom right, Fig. 7), which is very close to the timing resolution obtained when the track goes through the center of each pad. This result seems robust, since the pull-distribution of the SAT values is a normal Gaussian, with a mean and sigma value consistent with zero and one, respectively. Similar very good timing results were observed for all the tracks for which the four pads together provide geometrical acceptance of 100%.

6. Conclusions

The progress towards a well understood, robust, large-area, PICOSEC-Micromegas detector offering precise timing in the HL-LHC era and beyond was presented. Single channel prototypes have demonstrated an excellent timing resolution, of 76.0±0.4 ps for timing a single photoelectron and 24.0 ± 0.3 ps for timing the arrival of a MIP, using a CsI photocathode. The PICOSEC-Micromegas timing characteristics have been extensively studied in terms of detailed simulations and understood thoroughly in terms of a stochastic phenomenological model. A consistent and unbiased method was developed to estimate accurately the yield of photocathodes to photoelectrons, a parameter which affects drastically the timing resolution of the PICOSEC detector. A multi-pad PICOSEC-Micromegas device was constructed and tested in muon beam and preliminary results show that the timing resolution is 25 ps in the center of each pad and
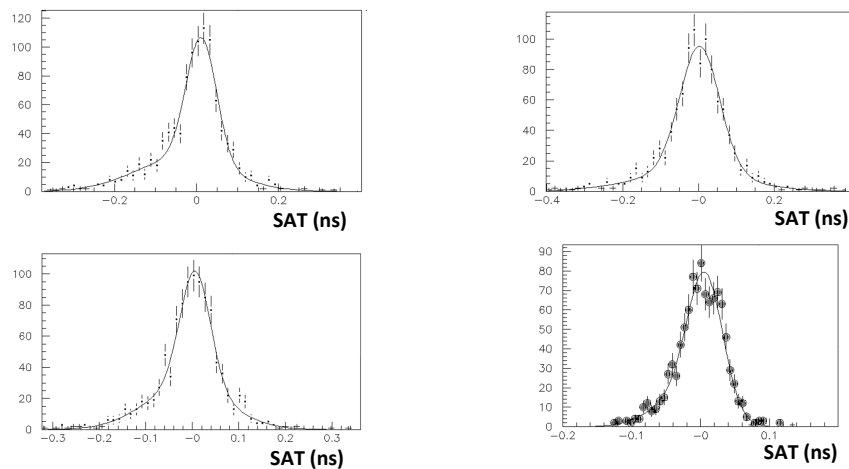
Figure 7. SAT distribution of each individual pad for tracks in the region between three pads, resulting to a timing resolution of 81 ps (top left), 70 ps (bottom left) and 86 ps (top right). SAT distribution combining the timing information from each pad and applying corrections (described in the text) resulting to 31 ps timing resolution (bottom right).

about 30 ps in the worst case that the produced p.e's. are shared between three pads.

7. Acknowledgments

References

[1] Papaevangelou T et al. 2018 Fast Timing for High-Rate Environments with Micromegas. In *EPJ Web Conf.*, volume **174**, https://doi.org/10.1051/epjconf/201817402002.

[2] Giomataris Y Rebourgeard P Robert J P and G Charpak. 1996 MICROMEGAS: a high granularity position sensitive gaseous detector for high particle flux environments. *Nucl. Instrum. Methods A*, **376**:29–35.

[3] Bortfeldt J et al for the RD-51 PICOSEC Collaboration 2018. PICOSEC: Charged particle timing at sub-25 picosecond precision with a Micromegas based detector. *Nucl. Instrum. Meth. A*, **903**:317–325.

[4] Cividec amplifier. https://cividec.at/index.php?module=public.product&idProduct=34&scr=0.

[5] Paraschou K. 2018 Study of the PICOSEC Micromegas Detector with Test Beam Data and Phenomenological Modelling of its Response. Master's thesis, School of Physics, Aristotle University of Thessaloniki, https://ikee.lib.auth.gr/record/297707/.

[6] Bortfeldt J et al. 2019 Modeling the Timing Characteristics of the PICOSEC Micromegas Detector. *arXiv preprint:* 1901.10779v1 [physics.ins-det].

[7] Schindler H and Veenhof R. Garfield**++** simulation of tracking detectors. https://garfieldpp.web.cern.ch/garfieldpp/.

[8] Sohl L. 2018 Robustness measurements of PICOSEC-Micromegas and study of different photocathode materials. In *Proc. of 9th Symposium on Large TPCs for Low-Energy Rare Event Detection.*